Accepted Manuscript

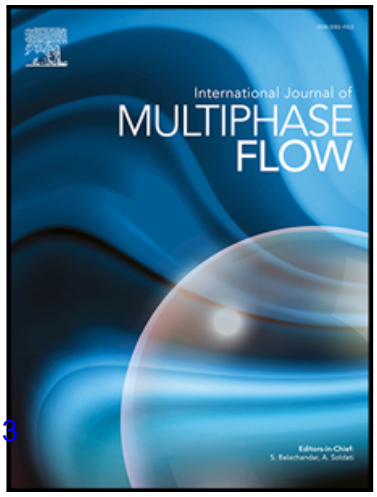

Effect of the scale resolution on the two phase coupling characteristics of high speed evaporating sprays using LES / Eulerian-Lagrangian methodologies

Li C., Crua C., Vogiatzaki K.

PII: S0301-9322(18)30644-X
DOI: https://doi.org/10.1016/j.ijmultiphaseflow.2019.06.013
Reference: IJMF 3060

To appear in: *International Journal of Multiphase Flow*

Received date: 4 September 2018
Revised date: 6 June 2019
Accepted date: 25 June 2019

Please cite this article as: Li C., Crua C., Vogiatzaki K., Effect of the scale resolution on the two phase coupling characteristics of high speed evaporating sprays using LES / Eulerian-Lagrangian methodologies, *International Journal of Multiphase Flow* (2019), doi: https://doi.org/10.1016/j.ijmultiphaseflow.2019.06.013

Highlights

- We perform a comprehensive evaluation of both the effect of the mesh structure and the grid resolution on two-phase flow modelling approaches using LES/Eulerian-Lagrangian frameworks.
- We present and explain trends of the mesh and grid effect on liquid and gas phase separately as well as on their coupling.
- For both mesh cases examined in this study, as the grid size close to the liquid core area is refined the droplet trajectories are becoming longer (higher liquid penetration) and more fuel droplets with higher velocities are present in the domain
- The grid size -if a variable Co number is used- affects the numerical time step which in turn affects how "often" the gas momentum equation is updated in respect to the time steps of the liquid phase and this can impose numerical oscillations for the prediction of the vapour phase.
- The droplet SMDs follow a linear relation in respect to the break-up coefficient (B1) which is particularly helpful in order to a priori select the coefficient in various high speed evaporating sprays if the experimental droplet size or the experimental Stokes number is known.
- We calculated the Stokes numbers in all examined cases and we found that they are less than 1, indicating that the particles' motion is tightly coupled to the motion of gas phase. This makes the calculations very prone to the selection of the break up model coefficient (B1) since the particle break up enhances this coupling.
- Since for multiphase flows the Kolmogorov scale cannot be considered as the only smallest flow scale and be used as scale separation criterion for the grid selection in a similar way done for single phase flows, we suggest that the numerical Stokes number can play the role of an additional grid selection parameter.

Effect of the scale resolution on the two phase coupling characteristics of high speed evaporating sprays using LES / Eulerian-Lagrangian methodologies

Li C., Crua C., Vogiatzaki K.*

Advanced Engineering Centre, University of Brighton, UK

Abstract

The physics of high-speed liquid jets injected in elevated temperature and pressure conditions are extremely complex due to the multi-scale and multi-phase flow characteristics. Large eddy simulations (LES) are widely applied for simulations of multi-phase flows because large scale mixing of ambient gas with the liquid vapour (when evaporation is occurring) is better captured than other traditional computational fluid dynamics (CFD) techniques, such as Reynolds Averaged Navier-Stokes (RANS). However, in order for the LES predictions to be accurate, in addition to the required numerical accuracy of the solvers and the effect of the sub-grid scale (SGS) models, the mesh dependence needs to be addressed especially for large scale applications that the mesh resolution is never sufficient to capture all scale range. Although previous works have presented the effect the grid has on the accuracy of the simulation results of sprays based on a "trial and error" basis, no insight of the dynamics of each phase was provided in the same conditions under different grids. In our work the novelty lies in the fact that the observed trends of each phase regarding the mesh are explained based on the code numerics (OpenFOAM) and linked to the physics of the flow. Moreover, we investigate for the first time the dependence of the the grid size on the mesh structure and the break up model coefficients. We aim to improve the understanding of the role of mesh refinement in multi-

*Corresponding author
Email address: k.vogiatzaki@brighton.ac.uk (Vogiatzaki K.)

phase coupling characteristics and to provide a guideline for mesh resolution requirements within LES/Eulerian Lagrangian approaches not only for high speed evaporating sprays but also for more general problems where a continuous and disperse phase are present.

Keywords: Spray dynamics; Two phase modelling; Eulerian-Lagrangian; LES; OpenFOAM

1. Introduction

Sprays are currently used in a wide range of applications in order either to distribute material over a cross-section (for example surface coating processes) and/or to generate liquid surface area (liquid atomisation and mixture formation in combustion systems). The successful utilisation of a spraying process in industry and the design of optimum injectors requires understanding of the physical-chemical processes and fluid mechanics that are involved. Despite recent advances in numerical methods for multiphase flows and high performance computing, the simulation of the exact evolution of the liquid structures for the total injection time is still a very challenging task. High speed sprays undergo atomisation and vaporisation processes which are extremely complex involving transient two-phase, turbulent flows at high pressures, with a wide range of temporal and spatial scales.

Various approaches are currently used to model these flows and can be broadly grouped into two categories. One approach follows an Eulerian-Lagrangian methodology (Amsden et al., 1989). The dispersed phase is modelled using a Lagrangian formulation, tracking individual droplet parcels. Appropriate algorithms are employed to interpolate the gas-phase properties at the Lagrangian parcel locations, and to distribute the interface source terms at the Eulerian grid. The second approach follows the Eulerian-Eulerian two-fluid methodology (Blokkeel et al., 2003), treating liquid and vapour as separate and interpenetrating phases. Conservation equations are solved for each one of these phases. A major disadvantage of this approach is the computational effort re-

quired as the droplet size distribution becomes wider. Some studies (Vallet et al., 2001, Yi and Reitz, 2003, Vujanović et al., 2016) have employed a hybrid approach, coupling Eulerian-Eulerian and Eulerian-Lagrangian methods. It is important to note that for any of these approaches, the accuracy of simulations depends upon the accuracy of the representation of the coupling of the two phases, in particular, when Large Eddy Simulation (LES), are used. For example in the recent work of Schmidt and Bedford, 2018 a framework for Eulerian-Lagrangian simulations has been suggested that controls the number of parcels used in order to succeed convergence.

The LES/Eulerian-Lagrangian approach is very appealing in comparison to other CFD tools for simulating complex liquid vapour mixing processes. LES is a less computationally demanding tool in comparison to Direct Numerical Simulations (DNS) but at the same time more accurate, being able to capture local unsteadiness, in comparison to Reynolds Averaged Navier Stokes (RANS). Our literature review reveals several groups using a RANS based Eulerian-Lagrangian approach (Senecal et al., 2003, Lucchini et al., 2009, Som and Aggarwal, 2010) for simulating high speed spray processes mostly targeting combustion related phenomena in Internal Combustion (IC) engines and aero engines. Comparisons between RANS and LES have been reported in many works (Zhou et al., 2011, Banerjee and Rutland, 2012, Som, Senecal and Pomraning, 2012, Blomberg et al., 2016). Through these studies it is demonstrated that although the global flow characteristics such as vapour penetration and liquid length have been fairly well predicted by RANS/Eulerian-Lagrangian methodologies, the instantaneous and local information of the dynamics of a high speed spray are better captured only using LES/Eulerian-Lagrangian methods.

More recently, different flavours of LES models have been applied for predicting spray and fuel mixing characteristics. A comprehensive review can be found in literature by Rutland, 2011. These models can be broadly classified as viscosity and non-viscosity based. Pomraning, 2000, Pomraning and Rutland, 2002 implemented an one equation non-viscosity dynamic structure model since it is known to be less dissipate compared to the viscosity based models, espe-

cially for coarse grids. The Smagorinsky based LES model (Som, Senecal and Pomraning, 2012, Xue et al., 2013) and dynamic structure sub-grid scale (SGS) model (Xue et al., 2013, Senecal et al., 2013, 2014) have also been widely implemented in the literature. They were observed to predict fairly well the spray structure and the global characteristics against experiments. Studies based on LES/Eulerian-Lagrangian approaches have recently start to be used (W.P. et al., 2014, Vogiatzaki et al., 2017) although most of the studies until toady have been focused on LES/Eulerian-Eulerian frameworks.

Open source and commercial softwares associated using these models become effective tools for the simulation of liquid spray and have been used by many researchers. Table 1 shows some of these previous studies for the experimental case that is known as "Spray A" and will be the focus of our study as well. It should be noted that apart from parameters such as grid resolution and turbulence model also the parameter B_1 is varied. This is the parameter that controls the droplet break up. Although this table indicates that there is a potential dependence on the grid size and the B_1 parameter, until now it is not clear in the literature what is the dependence of this parameter to the grid size as well as the rest of the SGS models.

Groups	Code	Grid size	B_1
Wehrfritz et al., 2012	OpenFOAM	0.0625-0.25mm	40
Senecal et al., 2013	CONVERGE	0.0625mm	5, 7
Bravo and Kweon, 2014	CONVERGE	0.25-2mm	12
Jangi et al., 2015	OpenFOAM	0.125-0.5mm	6
Senecal et al., 2014	CONVERGE	0.03125-0.5mm	5
Xue et al., 2013	CONVERGE	0.03125-0.5mm	5, 7

Table 1: Mesh size and breakup model constant used for modelling of ECN "Spray A" by different groups. B_1 is contant of KHRT breakup model (Reitz, 1987), expressing the breakup time of a liquid drop.

The major challenge is that the grid convergence concept in LES, especially

for multiphase flows is hard to be defined with strict criteria similar to single phase flows based on the Kolmogorov and Taylor scales analysis since the presence of multiple phases imposes a wider range of scales. In most cases, it is difficult to determine a priori where fixed grid embedding should be added and what is the appropriate resolution for the problem under consideration. Adaptive Mesh Refinement (AMR) enables tracking features much smaller than the overall scale of the problem providing adequate higher spatial and temporal resolution where needed. Thus, it is currently used in various studies (Som, Senecal and Pomraning, 2012, Xue et al., 2013, Senecal et al., 2013, 2014). This method adapts the accuracy of a solution within certain sensitivity threshold or flow region indication, dynamically, as the simulations progress. It allows for the user to solve problems that might be computationally intractable on a uniform grid. However, the disadvantage is that AMR increases computational and storage costs in comparison to a fixed grid approach which might be a problem when real life spray devices are considered, such as the combustion chamber in IC engines. Moreover, the adaptive refinement procedure is causing grid stretching which in turn results in numerical dissipation.

As an alternative to AMR, mesh refinement in the main spray developing regions based on fixed grids is used in many studies (Beck and Watkins, 2003, Senecal et al., 2003, Gong et al., 2010, Banerjee and Rutland, 2012, Battistoni et al., 2015) to accelerate the calculations and to facilitate the results' convergence. Within this approach the common practice of increasing the mesh resolution of LES (Banerjee and Rutland, 2012, Xue et al., 2013) following a "trial and error" approach or tuning the spray coefficients (Xue et al., 2013, Zamani et al., 2016) in order to capture the small scale structures is followed in the above studies. This approach, although gives accurate simulation results, is not predictive and a criterion needs to be established as to what should be the minimum grid requirements at the refinement region for optimum numerical and physical accuracy.

Our work aims to provide a better understanding of the mesh size requirements for Eulerian/ Lagrangian simulations within the LES framework as well

as the link between the grid resolution and other SGS parameters such as the break up model. We aspire to move one step ahead from the selection of grid resolutions based on "trial and error" approaches and establish criteria that will help us define the resolution a priori based on parameters that encapsulate the physics of the problem under consideration. These criteria can be very useful -if established- for industrially relevant simulations in order to succeed a quick turn over of simulations without the need of many sensitivity studies before deciding for the optimum grid. Within this paper the role of the mesh structure and the grid size is examined both for its effect on the resolution of the physical scales as well as on the numerical accuracy of the solver. The work is carried out using the LES/Eulerian-Lagrangian method based on a fixed mesh refinement in OpenFOAM. The effect of the small scales is applied on the LES flow field by adoption of the dynamic one equation model (Kim and Menon, 1995). It is a model that has not been used until now for the simulation of high speed sprays and it is based on the use of a locally adjusting model coefficient with a dynamic procedure.

The paper is organised in the following way. First we introduce in brief the governing equations of the two phase flow, including the LES filtered equations of the Eulerian phase and the equations for the Lagrangian Particle Tracking (LPT) method of the dispersed phase. Then the experimental and numerical setups are given in Section 3. Finally, we present the results which are separated in two parts, i.e. the global characteristics of liquid and vapour penetrations and the individual analysis of both the liquid and gas phases. Conclusions and suggestions for future work are presented in the last section (Section 5).

2. Governing equations and sub-grid scale models

In LES the turbulent flow is decomposed into coherent large scales, which are directly resolved, and smaller scales that are unresolved and require modelling. To decompose the scales, a spatial filter is applied to the dependent variables $\Psi = \widetilde{\Psi} + \Psi''$ with $\widetilde{\Psi} = \overline{\rho\Psi}/\overline{\rho}$ where $\bar{\cdot}$ and $\widetilde{\cdot}$ denote filtered and Favre-filtered

quantities, respectively. Applying the filter operation to the governing equations describing the conservation of mass momentum and energy, the Favre-filtered equations read

$$\frac{\partial \overline{\rho}}{\partial t} + \frac{\partial \overline{\rho}\widetilde{u}_j}{\partial x_j} = \overline{S}_\rho \tag{1}$$

$$\frac{\partial(\overline{\rho}\widetilde{u}_i)}{\partial t} + \frac{\partial(\overline{\rho}\widetilde{u}_i\widetilde{u}_j)}{\partial x_j} = \frac{\partial}{\partial x_j}(-\overline{p}\delta_{ij} + \overline{\rho}\widetilde{u}_i\widetilde{u}_j - \overline{\rho u_i u_j} + \overline{\sigma}_{ij}) + \overline{S}_{u,i} \tag{2}$$

$$\frac{\partial(\overline{\rho}\widetilde{h}_t)}{\partial t} + \frac{\partial(\overline{\rho}\widetilde{h}_t\widetilde{u}_j)}{\partial x_j} = \frac{\partial \overline{p}}{\partial t} + \frac{\partial}{\partial x_j}(\overline{\rho}\widetilde{u}_j\widetilde{h} - \overline{\rho u_j h} + \frac{\overline{\lambda}}{\overline{c_p}}\frac{\partial \overline{h}}{\partial x_j}) + \overline{S}_h \tag{3}$$

where $\overline{\rho}$, $\widetilde{u}_i$, $\overline{p}$ and λ denote the density, velocity component in i direction, pressure and heat conductivity respectively. Here, the total enthalpy is the sum of the absolute enthalpy and specific kinetic energy $\widetilde{h_t} = \overline{h} + \frac{\widetilde{u}_i\widetilde{u}_i}{2}$ and the filtered viscous stress tensor is defined as

$$\overline{\sigma}_{ij} = \overline{\mu}(\frac{\partial \widetilde{u}_i}{\partial x_j} + \frac{\partial \widetilde{u}_j}{\partial x_i} - \frac{2}{3}\frac{\partial \widetilde{u}_i}{\partial x_j}\delta_{ij}) \tag{4}$$

where $\overline{\mu}$ is the dynamic viscosity of the fluid. Each equation contains a source term for mass ($\overline{S}_\rho$), momentum ($\overline{S}_{u,i}$) and energy ($\overline{S_h}$) that incorporates the interaction of the continuous (gas) with the dispersed (liquid) phase.

The Lagrangian Particle Tracking (LPT) technique is employed for the liquid part of the simulations. The spray is considered as a discrete phase comprising of a large number of parcels that are transported using Newton's second law. The equations of the dispersed liquid phase are expressed as:

$$\frac{dx_p}{dt} = u_p \tag{5}$$

$$\frac{du_p}{dt} = \frac{u_{rel}}{\tau_p} \tag{6}$$

where x_p is the position vector of the particle and u_p is the particle velocity. The relative velocity $u_{rel} = u_g - u_p$, where u_g, u_p are the velocities of the gas (interpolated to the particle position from the adjacent cells) and the droplet

respectively. The term τ_p is the droplet response time. In the current study, simulations of particles are done using the equation of motion which assumes that the force acting on a droplet is due to drag as:

$$\frac{1}{6}\rho_p \pi d_p^3 \frac{du_p}{dt} = \frac{1}{2}(u_g - u_p)|u_g - u_p|\rho_g C_D \frac{\pi d_p^2}{4} \tag{7}$$

where d_p is the diameter of particle and C_D is the droplet drag coefficient that is defined by

$$C_D = \begin{cases} \frac{24}{Re_p}(1 + \frac{1}{6}Re_p^{2/3}), & Re_p < 1000 \\ 0.424 & Re_p \geq 1000 \end{cases} \tag{8}$$

A Rosin-Rammler distribution (Bailey et al., 1983) is used in order to provide the initial particle distribution. The injected droplets have a diameter in the range $1\mu m \leq d \leq 90\mu m$.

The liquid evaporation model, based on the ideal gas assumption and including a boiling model based on Zuo et al., 2000 and Spalding's expression (Spalding, 1964), is used for the calculation of the droplet mass evaporation rate. When convection effects are taken into account, Ranz and W. R. Marshall, 1952*a*; Ranz and W. R. Marshall, 1952*b* proposed an expression based on the particle Reynolds number Re_p and the Prandtl number (Pr).

$$Nu_p = 2.0 + 0.6Re_p^{1/2}Pr^{1/3} \tag{9}$$

A Prandtl number $Pr = 0.7$ is used in this work.

To model the spray breakup, both the Kelvin-Helmoltz (KH) and Rayleigh-Taylor (RT) mechanisms (Reitz, 1987) are accounted for through a standard KHRT model. As reported in our literature review in the introduction, KHRT has been used in various studies of sprays both within LES and RANS (Wehrfritz et al. 2012, Xue et al. 2013, Senecal et al. 2013, Senecal et al. 2014, Battistoni et al 2015). The breakup parameter B_1 included in the model influences the rate of separation and depends on the nozzle and the spray's properties (Magnotti and Genzale, 2017). The values of $B_1 = 3$, and 15, are adopted for the simulations

using mesh 2 and mesh 1 respectively in Fig. 1. The choice of these two values, as will be explained in the next sections, is based on a detailed sensitivity analysis (see Appendix D) in order to obtain the best results for each mesh. As we will demonstrate the choice of different mesh structures imposes the need of different B_1 parameters in order to succeed similar accuracy at the same grid resolution. In other words in this study we focus on comparing primarily mesh structures and grid resolutions and the use of the rest of parameters is just the result of this variation

A dynamic one-equation model (Kim and Menon, 1995) is adopted by solving the transport equation for sub grid-scale kinetic energy for the closure of the SGS turbulent viscosity term

Additional details for the models and the exact coefficients used are provided in the Appendix.

3. Experimental and numerical set up

Numerical simulations are compared with experiments carried out in a constant volume pre-burn vessel at Sandia National Laboratories. The ECN "Spray A" conditions simulated in present work are provided in Table 2. Further experimental information can be referred to Sandia National Laboratories, 2018, Senecal et al., 2007, Pickett et al., 2010.

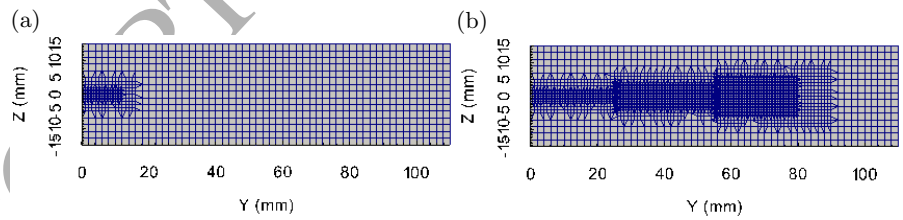

Figure 1: Grid mesh 1 (a) and mesh 2 (b) used for LES simulations of Spray A conditions.

In order to resolve numerically the flow near the injector and along the spray development region, a fixed grid embedded refinement is employed at two mesh configurations as shown in Fig. 1. Mesh 1 imposes refinement at the

Ambient gas temperature	900 K
Ambient gas pressure	near 6.0 MPa
Ambient gas density	22.8 kg/m^3
Ambient gas oxygen	0% O2 (non-reacting)
Ambient gas velocity	Near-quiescent, less than 1 m/s
Fuel injector outlet diameter	0.090 mm
Number of holes	1 (single hole)
Discharge coefficient	Cd = 0.86
Fuel	n-dodecane
Fuel injection pressure	150 MPa
Initial fuel temperature	363 K (90°C)
Duration of injection	1.5 ms
Total mass injected	3.5 mg
Fuel density	750 kg/m^3

Table 2: Summary of ECN "Spray A" conditions (Sandia National Laboratories, 2018, Senecal et al., 2007, Pickett et al., 2010).

region of the maximum liquid penetration (up to 10 mm along Y axis, the fuel injection direction) based on experimental data. Mesh 2 is refined (up to 80 mm, along Y axis) in region including both the liquid and the vapour lengths. It should be noted that due to the Eulerian-Lagrangian nature of the code the grid affects directly the gas phase and indirectly (through the numerical coupling) the Lagrangian phase. The choice of two mesh refinement structures allows us to separate the effect of the mesh on the liquid/gas coupling from its effect on the vapour development. Three levels of mesh refinement with a grid size factor 0.5 are implemented in the computational domain $-0.015\,\mathrm{m} \leq X \leq 0.015\,\mathrm{m}$, $0 \leq Y \leq 0.11\,\mathrm{m}$, $-0.015\,\mathrm{m} \leq Z \leq 0.015\,\mathrm{m}$. The smallest grid size appears in the inner most mesh refinement region. The total number of cells and the required computing resources of each case are given in Table 3. The calculations in this study are run in parallel on distributed memory machines using the message

Case	Minimum mesh size	Number of cells	Run time
1 (mesh1)	$0.5mm$	20,000	0.5hs
2 (mesh1)	$0.25mm$	100,000	2.5hs
3 (mesh1)	$0.125mm$	1,000,000	20hs
4 (mesh2)	$0.25mm$	700,000	15hs
5 (mesh2)	$0.125mm$	5,000,000	100hs

Table 3: Summary of simulated cases.

passing interface (MPI).

It should be pointed out that the grid quality affects both the solver efficiency and the accuracy of the solutions. Our research uses the hexahedral mesh, which is the most commonly used mesh in OpenFOAM studies. In order to maintain stability, time accuracy is set to first order by running fully implicit. The time step is calculated based on the Courant number criterion: $\mathrm{Co}_{\max} = u\Delta t/\Delta x$ where Δx is the grid size while Δt is the time step. For the calculations presented in the results section the $\mathrm{Co}_{\max} = 0.1$ is used. A second-order-accurate spatial discretisation scheme is used for the governing conservation equations. Both the divergence and the Laplacian terms are calculated using a Gaussian Linear scheme. The transport equations are solved using the pressure implicit with splitting of operators (PISO) method.

The method of Lagrangian Particle Tracking (LPT) is used to record the movement of liquid parcels as follows: (a) Initially each parcel moves until it reaches a cell boundary or for the entire time step (Δt or dt) if it remains in the same cell (b) If the parcel changes cell, the time it took to move out of the first cell is calculated and the parcel properties are updated based on this time (c) The momentum change is added to the cell that the parcel has been in (d) If the parcel still has time left to move, step (a) is repeated. It can be seen that based on this algorithm the grid size, apart from its profound role in resolving turbulent scales, also affects the way the parcels move and how often the momentum equation is updated. It is expected that for smaller grid sizes

the parcel properties are updated in shorter time scales than in larger grids although this is also dependent on the simulation time step. In the current study a injection rate of 40 million particle per second (PPS) is used following a sensitivity analysis (see Fig. 23 in Appendix C).

4. Results and discussion

4.1. Liquid and vapour penetrations

This section presents the results of spray simulations under "Spray A" conditions using the two mesh configurations in Fig. 1. The spray global characteristics, i.e. liquid and vapour penetrations, are initially compared with experimental data from Sandia National Laboratories, 2018 and Senecal et al., 2007. Liquid penetration is defined as the axial location encompassing 95% of the injected mass at that instant in time. Vapour penetration at any time is determined from the farthest downstream location of 0.05% fuel mass-fraction contour.

(a) (b)

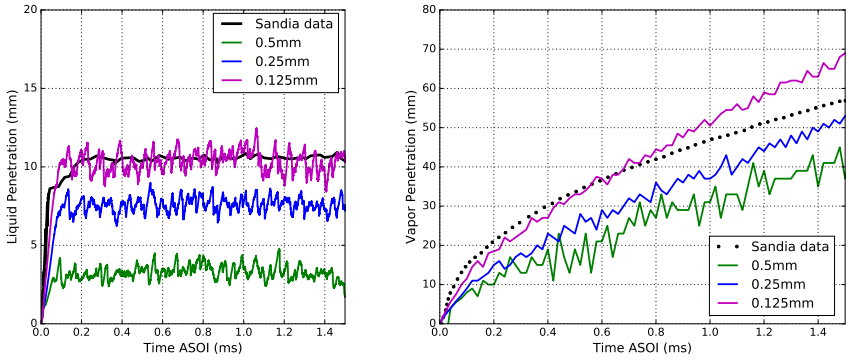

Figure 2: Effect of grid size on liquid (a) and vapour (b) penetrations for "Spray A" conditions (Sandia National Laboratories, 2018, Senecal et al., 2007, Pickett et al., 2010) on mesh 1.

Figures 2 and 3 show the liquid and vapour penetrations as a function of time from measurements and predictions, using different grid sizes 0.5 mm, 0.25 mm and 0.125 mm (three grid resolutions for mesh 1 and two grid resolutions for

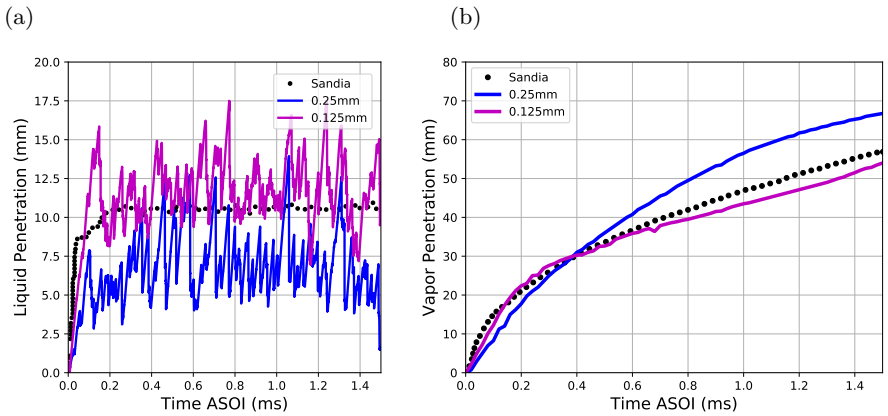

Figure 3: Effect of grid size on liquid (a) and vapour (b) penetrations for "Spray A" conditions (Sandia National Laboratories, 2018, Senecal et al., 2007, Pickett et al., 2010) on mesh 2.

mesh 2, referring to the minimum cell size obtained by mesh refinement in Fig. 1). The plots show that 0.5 mm and 0.25 mm grid resolutions are not sufficient to reproduce the liquid and vapour penetration characteristics on both mesh configurations. As the grid is refined further, the predicted spray penetrations approach the experimental data at the grid resolution of 0.125 mm, in good agreement with previous LES studies (Banerjee and Rutland, 2012, Som, D'Errico, Longman and Lucchini, 2012, Xue et al., 2013). Although liquid penetrations are under predicted when an insufficient grid resolution is used, their trends are different for the prediction of vapour penetration between mesh 1 and 2. The results show that the initial vapour penetrations are under-predicted for mesh 1 but over-predicted for mesh 2. Also noticeable oscillations occur at the liquid penetrations using mesh 2 (see Fig. 3 (a)). To further analyse and understand the sources of the oscillations, we derived the particle displacement equation from Eqs 5 and 6 as:

$$\begin{aligned} x_p &= (\frac{u_{rel}}{2\tau_p})dt^2 + c_1 dt + c_2 \\ &= \frac{(u_g - u_p)\cdot 18\nu \cdot C_D}{2d_p^2\rho_g} dt^2 + c_1 dt + c_2 \end{aligned} \tag{10}$$

where c_1 and c_2 are constants, ν and ρ_g are the kinematic viscosity and

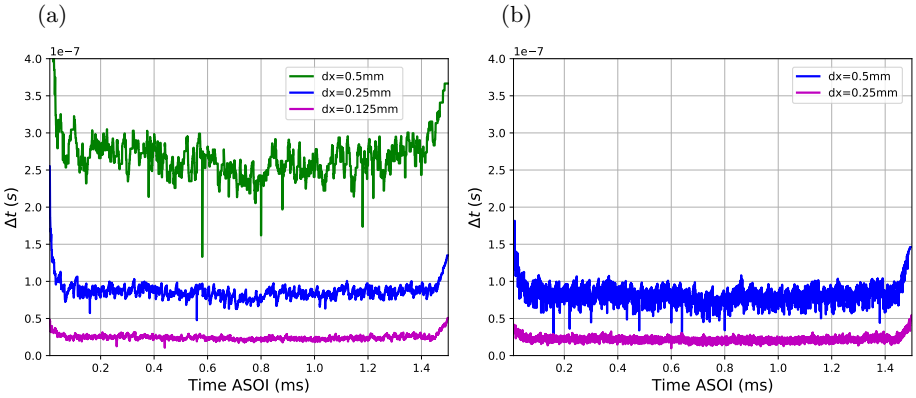

Figure 4: Time step variation over time for (a) mesh 1 (b) mesh 2

density of fluid. A standard drag factor $C_D = 0.424$ is used in this work. It can be seen from the above relation that several important factors might affect the instabilities of the liquid penetration. These factors can be summarised as: (a) The time step (b) the relative speed between the particle and gas $(u_g - u_p)$ which is affected by the modelled small scales (c) The coupling of the two phases, and (d) The droplet size d_p. Further investigation of their effect is presented in the following paragraphs. One important note is that sometimes oscillating results in Eulerian-Lagrangian studies are attributed to the use of insufficient particle numbers in the simulations. However, this is not the case in our study since a particle number sensitivity study has been performed and shown in Appendix C.

Under the limit of maximum Courant number $C_o < 0.1$, a variational time step (see Fig. 4) is used in order to enhance numerical stability on the two mesh structures. The order of magnitude of the time step $\mathrm{O}(1.e-7)$ is comparable to that used in other published studies (Wehrfritz et al., 2012) under the same conditions. The plots of Fig. 4 show smaller oscillations appearing in Δt when the grid size decreases on the two mesh configurations. With the same grid size, the higher time step oscillations of mesh 2 than mesh 1 are likely to triger larger oscillations on the liquid penetration in Fig. 3 (a). However it cannot be

considered as the only reason of oscillations since the grid refinement results in lower time step variations but equally large liquid penetration variations. Thus, two more factors will be examined in the following figures i.e. the effect of the modelled small scales ($u_g - u_p$) and the droplet sizes that are produced in different meshes based on the effect that the grid size and the mesh structure has on the evaporation and the break up process within the Eulerian-Lagrangian framework.

Starting with the coupling effect, in order to better quantify the interaction of the two phases, the Stokes number (Stk), based on the smallest resolved scale (the smallest grid size) of the Eulerian phase and the average Sauter Mean Diameter (SMD) of the droplets of the Lagrangian system in Fig. 5, is calculated and presented in Table 4. Further explanation of the Fig. 5 will be provided in the next paragraphs however here we just use it in order to clarify the calculation of the numbers in Table 4. The Stokes number is defined as the characteristic response time of the fluid divided by the characteristic response time of the particle. If the Stokes number is small (less than 1), this also suggests that mixture theory can be used instead of full multiphase approach as there is little relative motion between phases locally. If the Stokes number is larger than 1, the particles are not influenced considerably by the gas phase. Their response time is longer than the time the gas has to act on it and so the particles will pass through the flow without much deflection in its initial trajectory. In turbulent flows the fluid time scale may be the rotation time of a characteristic eddy. For all examined cases, the Stokes numbers are less than 1, indicating that the particles' motions are tightly coupled to the motion of gas phase. It also can be seen that the Stokes numbers are evidently smaller with mesh 2 than mesh 1. This implies that the same grid size in reality imposes a stronger numerical coupling of the two phases for mesh 2 and thus the dynamics of the liquid (Lagrangian) phase are considerably influenced by the numerical and physical instabilities of the gas (Eulerian) phase.

In order to examine the effect of the predicted droplet sizes on the instabilities of liquid phase we revisit Fig. 5 which shows the SMD of the droplets

case	Stokes number (Stk)	Grid size ($dx,\ mm$)	Particle diameter (SMD,$\times\ 10^{-6}\ m$)
case 1 (mesh 1)	0.19	0.5	2.22
case 2 (mesh 1)	0.35	0.25	2.12
case 3 (mesh 1)	0.81	0.125	2.29
case 4 (mesh 2)	0.02	0.25	0.52
case 5 (mesh 2)	0.06	0.125	0.62

Table 4: Summary of the Stokes (Stk) numbers.

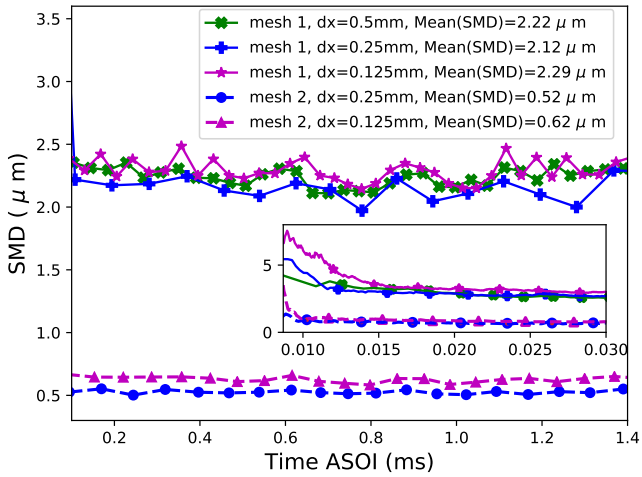

Figure 5: Sauter Mean Diameter with different grid sizes of mesh 1 and mesh 2. The embedded plot shows the SMD values close to the nozzle in early stage after the injection instant. The breakup coefficient value $B_1 = 15$ is used for mesh 1 and $B_1 = 3$ for mesh 2.

during injection in various grids over time. It can be seen that the mean SMD with mesh 1 is around $(2.1 - 2.3)\mu m$ and it is larger than the SMD predicted for mesh 2 ($(0.5 - 0.6)\mu m$) when the phase that the liquid penetration is stabilised to 10 mm penetration is examined. Although the SMDs vary with the mesh structure they remain the same as the grid changes. This is consistent with the observations of more noticeable oscillations of liquid penetration with

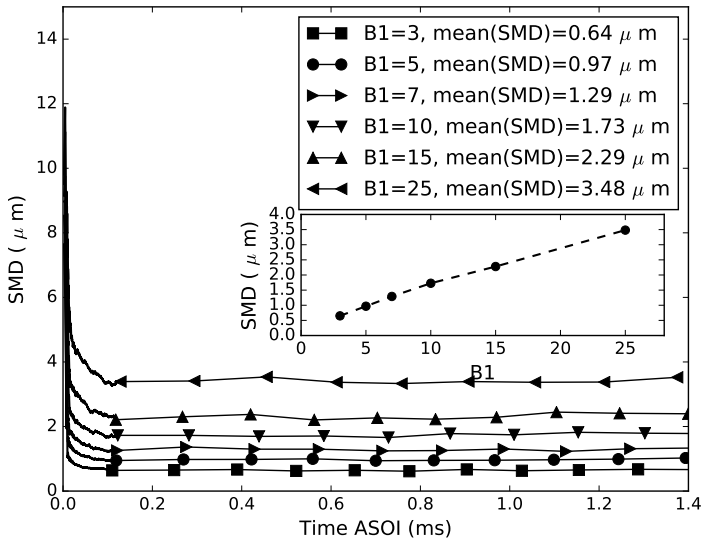

Figure 6: Sauter Mean Diameter with different values of the breakup coefficient B_1 at 0.125mm with mesh 1. The embedded plot shows an approximate linear function between SMD and B_1. The same observations are obtained with mesh 2.

mesh 2 than mesh 1, regardless of the grid size under the same refinement structure. It is thus estimated that the smaller droplet size of liquid phase at the relatively "stable" stage after injection, plays a dominant role for triggering the oscillations of liquid phase of Fig. 3, since it imposes a stronger coupling degree between the two interacting phases on mesh 2. Moreover, it can be seen that after injected in the high pressure high temperature gas environment, the size of the droplets is quickly reduced and finally stabilised at a small SMD diameter after breakup time around $t = 0.015$ ms with mesh 1 and after a shorter breakup time around $t = 0.009$ ms with mesh 2 as shown in the embedded figure.

One factor that affects the prediction of the breakup time and droplet size is the breakup coefficient B_1 as it is demonstrated in Fig. 6. For the simulations presented in Fig. 5 the value $B_1 = 3$ is used on mesh 2 and $B_1 = 15$ on mesh 1. In Fig. 6 it can be seen that as the B_1 is increased the SMD increases as

expected. The embedded plot displays an approximate linear function between SMD and B_1 at the relatively "stable" stage after $t = 0.1$ ms. The same phenomenon is observed on mesh 2. For $B_1 = 3$ for mesh 1 a similar to mesh 2 value of SMD is predicted for the same grid resolution 0.125 ms. However when this value was used for the simulation in mesh 1 the liquid penetration was considerably over predicted. This is why two different B_1 values were chosen for the two meshes. A detailed sensitivity analysis of the liquid and vapour penetration predictions to the B_1 parameter is shown in Appendix D

The linear relationship between the breakup coefficient and the droplet size provides a potential a priori selection criterion of the B_1 coefficient if either the Stokes number or the actual SMD of the droplets is known from experimental data. Previous studies have also shown convergent results by calibrating the KHRT breakup model's coefficient B_1 based on their selected Eulerian mesh (Som, D'Errico, Longman and Lucchini, 2012, Xue et al., 2013). This work confirms the conventional method and further explains the effect of B_1 as a determinant factor for the SMD of particles.

Oscillations are also observed in the vapour penetrations with mesh 1 (Fig. 2b) although the trend is opposite to the trend of the oscillations of the liquid penetration and thus it is believed they have different origins. These oscillations are more noticeable at the simulations with the coarser mesh (0.5 mm), and gradually fade out at the fine mesh (0.125 mm). It is reminded that based on the experimental data the liquid penetration reaches only up to 10 mm, while the rest of the vapour penetration is handled solely by the Eulerian solver which implies that the vapour phase oscillations are associated with numerical inaccuracies because of the inadequate grid resolution.

This section mainly examined the effect of the mesh size on the convergence of the simulation results against the experimental data. A good agreement is succeeded when a resolution of 0.125 mm is used at the region that the liquid phase is present. A better resolution at the Eulerian phase (after the 10 mm downstream), although improves to a certain extent the vapour penetration, does not affect the average length of the liquid penetration, only the droplet

SMD. The difference in the SMD though induces fluctuations at the liquid penetration We also analysed in detail the potential sources in physics and numerics leading to the instabilities of global spray characteristics of the two phases within LES/Eulerian-Lagrangian frame. In the case of the vapour penetration fluctuations, they are more connected to the numerics of the code (LPT method) and the grid resolution. For the liquid penetration it is harder to separate the physical from the numerical fluctuations. It is found that the droplet size has a considerable effect on the instabilities of the liquid phase. Higher fluctuations are mostly associated with smaller droplet sizes present especially for mesh 2, implying that the finer grids at the Eulerian phase induce a coupling of the Eulerian and Lagrangian phase in a way that evaporation and break up is enhanced. This is reflected in the Stokes numbers calculated from the flow characteristics. The following sections are focused on further investigations of these observation by examining the effect of mesh resolution separately on the two phases of the high-speed evaporating spray conditions and the examination of the droplet statistics.

4.2. Analysis of liquid phase

Figures 7 and 8 show the influence of the mesh on the development of droplets along the direction of the mass flow injection at two time instances: $t = 0.8$ms (mid-injection duration) and $t = 1.5$ ms (end of injection). A first observation is that the liquid particles for all grid sizes and mesh structures are experiencing a longer trajectory at $t = 0.8$ ms than $t = 1.5$ ms. This is expected since at the end of injection, the injection mass flow rate is reduced to zero, which also results in a lower parcel velocity. Moreover, for all cases, as the grid size at the liquid area is refined the droplet trajectories are longer along the direction of fuel mass injection and more fuel droplets with higher velocities are present. Looking at the end of injection, it can be seen that for grid size 0.25 mm the liquid penetrates considerably further for mesh 1 than mesh 2. However, for grid size 0.125 mm the liquid penetration is similar for both meshes implying a convergence of the liquid penetration length for sufficiently small grid size at

the liquid core area. The accurate prediction of droplets at the end of injection is important since this will affect the prediction of emissions from unburned fuel in case the simulations reproduce sprays that are used in combustion devices as in the case of the experimental data used. The velocity distributions of the droplets in the two meshes with the same grid resolution at mid-point present differences. A continuous liquid core is present up to 12 mm while for mesh 2 the liquid core reaches up to 10 mm and only some clouds of droplets travel further downstream.

(a)

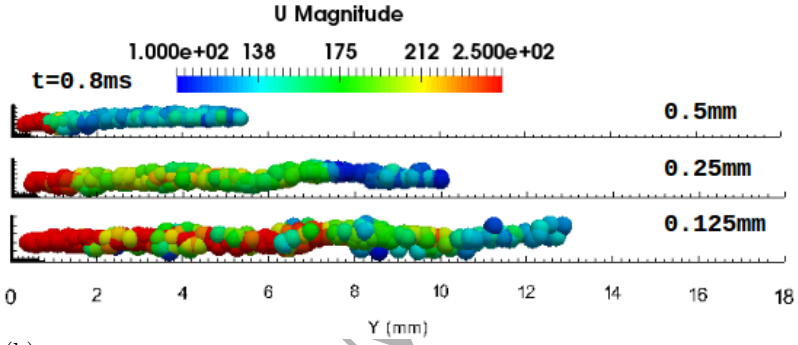

(b)

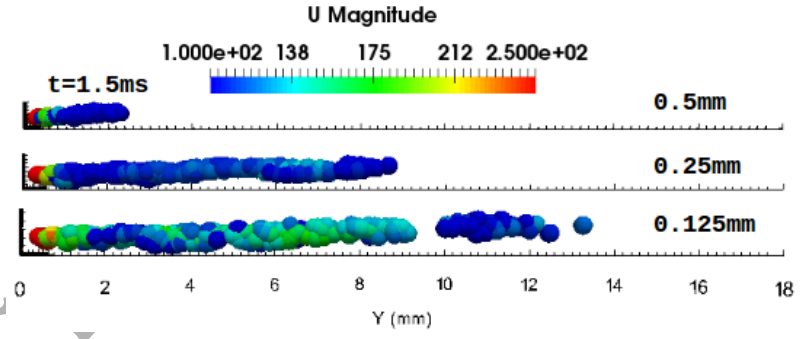

Figure 7: Effect of the grid size on the development of particles at $t = 0.8ms$ (a) and $t = 1.5ms$ (b) for Spray A conditions on mesh 1. The parcels are coloured based on the velocity magnitude. The same note for Fig. 7, 8, 12, 13: PPS (parcels per second) =40 million is used in this study. The particles are plotted with a maximum sample number 5000 and uniform spatial distribution of glyph mode to avoid as much as possible the display of particle overlapping projected from a 3D physics to a 2D plot.

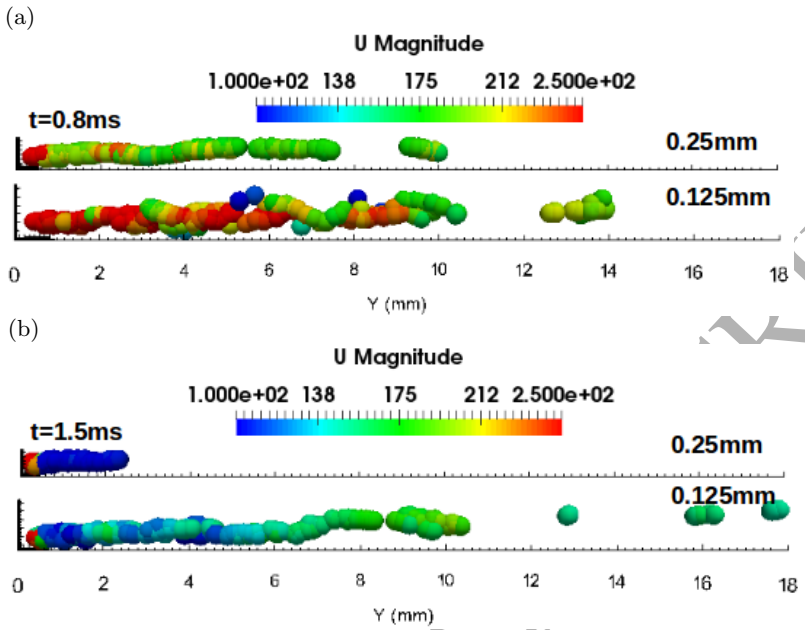

Figure 8: Effect of the grid size on development of particles at $t = 0.8ms$ (a) and $t = 1.5ms$ (b) for Spray A conditions on mesh 2. The parcels are coloured based on their velocity magnitude.

One way of explaining the previously described behaviour is by using the principle of momentum conservation. Ignoring the exchange of mass at two successive short instants, the momentum conservation for gas and liquid phase can be applied in each Eulerian cell:

$$m_p u_{p_A} + \rho_g (dx)^3 u_{g_A} = m_p u_{p_B} + \rho_g (dx)^3 u_{g_B} \tag{11}$$

$$m_p (u_{p_B} - u_{p_A}) = \rho_g (dx)^3 (u_{g_A} - u_{b_B}) \tag{12}$$

where m_p is the mass of the particle, u_{p_A} is initial velocity of the particle, u_{p_B} is the final velocity of the particle, ρ_g is the density of the gas phase, dx the mesh size, u_{g_A} is the initial velocity of the gas and u_{g_B} is the final velocity of the gas. When the same amount of momentum $m_p(u_{p_B} - u_{p_A})$ is lost from

an active particle in a cell, the change of the velocity of the passive gas phase ($u_{g_B} - u_{g_A}$) within a larger cell size is less. This in turn affects the follow up movement of the parcels and in particular the ones with smaller Stokes numbers that the two phase coupling is stronger (see Table 4). Thus, as we refine the grid the velocity of the gas phase changes more rapidly resulting in longer liquid penetration and longer particle paths with higher velocities. In other words the mesh size has an important effect on the inertia dynamics of droplets along the direction of mass flow injection, due to momentum conservation between the two phases. It should be pointed out that Eqs. 11 and 12 refer only to one particle and thus should be viewed only as a simplified initial approximation of the conditions in a cell.

It should be noted also that, the Eulerian phase can only be updated with information from the Lagrangian phase after an Eulerian time step Δt is finished while the Lagrangian time sub-steps are always smaller or equal to the Eulerian time step. Thus, it can be seen from Fig. 4, that a longer time interval Δt is taken with coarser mesh for updating the contribution of liquid phase on the Eulerian phase, and consequently more noticeable oscillations are introduced into the statistics (see vapour penetrations of Fig. 2b) of the Eulerian phase with the same mesh structure because of the time lag between the Eulerian and the Lagrangian time steps.

The velocity of the droplets should always be viewed along with their size distribution that, as explained in the previous sections, affects the degree of coupling with the underlying flow, and of course the temperature which is associated with the degree of evaporation.

Figures 9 and 10 show the average mass, momentum and kinetic energy time evolution of the particles in the Lagrangian part for the two different meshes. It can be seen that all three quantities increase as the grid size decreases with both mesh 1 and 2. This is in good agreement with the observations of longer trajectories (see Fig. 7 and 8) of moving particles. It also confirms our observations based on Eq. 11. For smaller cell sizes "more" momentum is transferred to the gas phase and this means that the gas phase locally accelerates

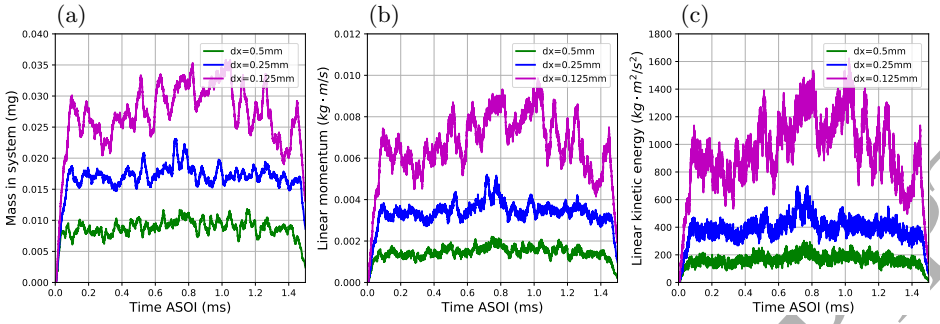

Figure 9: Effect of the grid size on the fuel (a) mass; (b) linear momentum; (c) linear kinetic energy in the Lagrangian system for mesh 1.

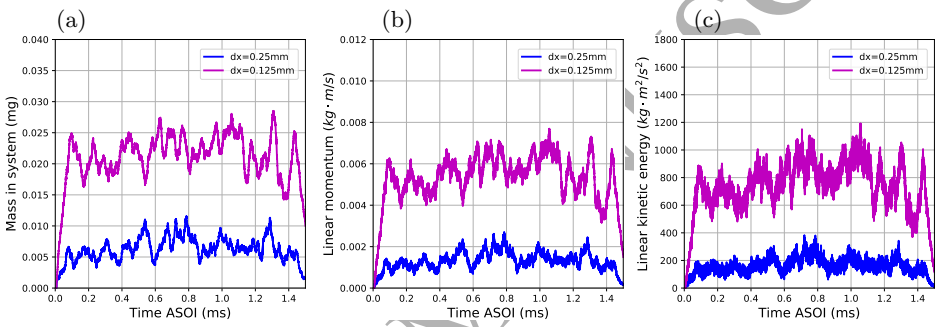

Figure 10: Effect of the grid size on the fuel (a) mass; (b) linear momentum; (c) linear kinetic energy in the Lagrangian system for mesh 2.

quicker which in turn moves smaller particles (with small Stokes number) as the ones present in mesh 2, quicker. Some additional conclusions from Figs 9 and 10 are that for grid size 0.25 mm the magnitude of the kinetic energy and momentum depends considerably on the mesh structure. For mesh 2 the momentum and the kinetic energy is smaller. On the contrary at grid size 0.125 mm convergence of these quantities is noticed.

Since momentum and kinetic energy both depend on the mass, Fig. 11 is also included in order to separate this effect given that the average SMD is higher in mesh 1. The results show that the liquid cores have the same mean velocity at grid size 0.125 mm where the converged liquid penetrations are obtained on the two mesh configurations. This is also true for grid resolution of 0.25 mm

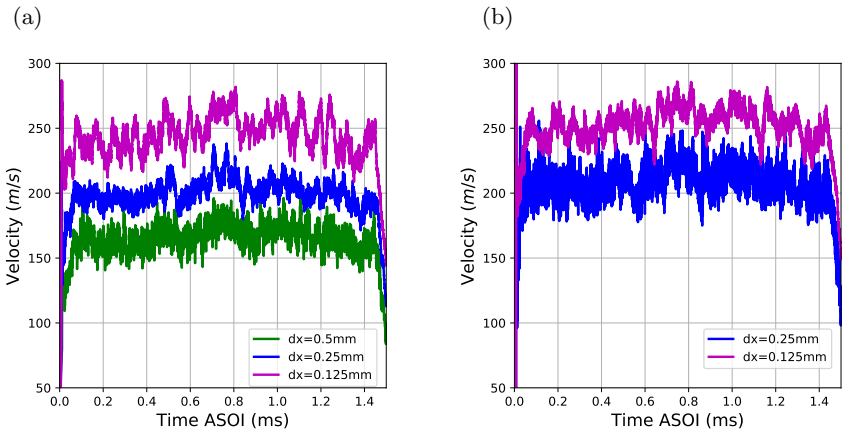

Figure 11: Effect of mesh size on the mean velocity of fuel particles in Lagrangian system along the direction of mass flow injection for Spray A conditions on mesh 1 (a) and mesh 2 (b).

which indicates that the differences in the momentum and kinetic energy is mostly related to the mass of the liquid phase (droplet size) rather than the velocity. Looking at Figs 9 and 10 the total mass of the Lagrangian particles at each instant is considerably lower for mesh 2 than for mesh 1 which is also consistent with Figs 2b and 3b that show a greater vapour penetration for mesh 2 at 0.25 mm resolution but under-prediction of the same quantity for mesh 1. It is also consistent with Fig. 5 which shows the SMD of the droplets during injection in various grids over time and indicated lower SMD for mesh 2.

The results in Figs 12 and 13 show the process of droplets gradually warming up from the initial low injection temperature (363 K) towards the high temperature of the gas phase (900 K). The colour mapping is divided by the liquid fuel's boiling point (489 K for n-dodecane). The boiling point may greatly alter the fuel-air mixing process and result in several characteristic changes, including: (1) spray angle increase; (2) droplet SMD decrease with increasing fuel temperature and decreasing pressure; (3) fast fuel flash vaporisation; and (4) a decrease in downstream central spray width. These changes can have a significant impact on the fuel distribution and mixing in an industrial engine application. Start-

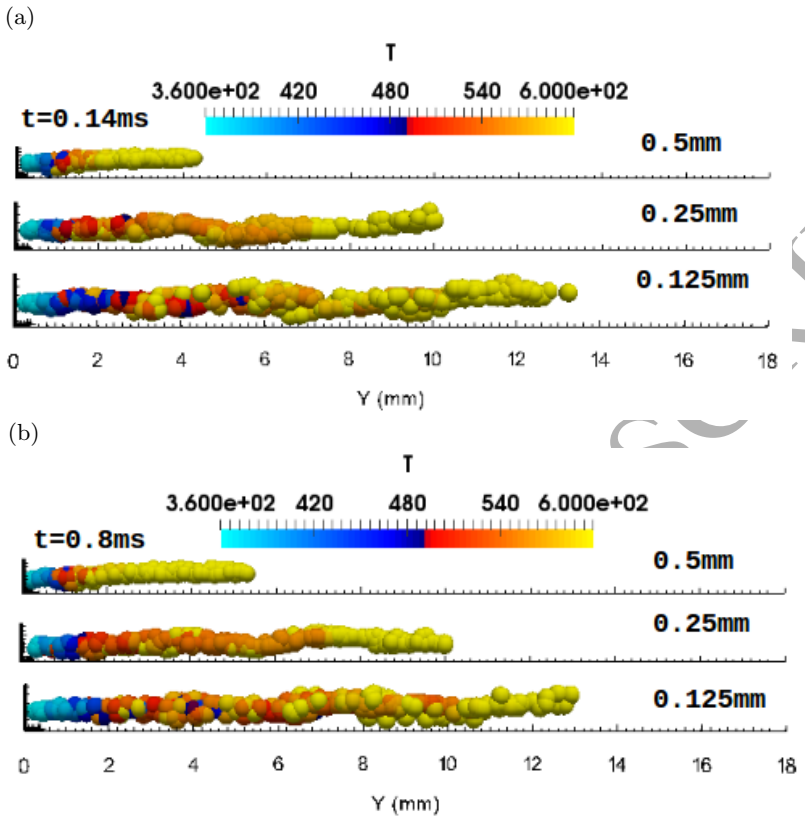

Figure 12: Effect of the grid size on development of particles at $t = 0.8$ms (a) and $t = 1.5$ms (b) for Spray A conditions on mesh 1. The parcels are coloured based on their temperature magnitude.

ing from the liquid injection position, the very short paths of moving particles, coloured blue, indicate the evaporation transition process from liquid phase to gas phase that occurs on the surface of liquid core or droplets.

After this, the liquid fuel reaches quickly a temperature above its boiling temperature, coloured by red and yellow, where the transition from liquid to gas phase occurs as boiling process. It is reminded that boiling is the phase change process that takes place at or above the boiling temperature and it occurs below the liquid surface. It appears that the liquid fuel is experiencing a fairly longer boiling rather than evaporating process. This observation is the same

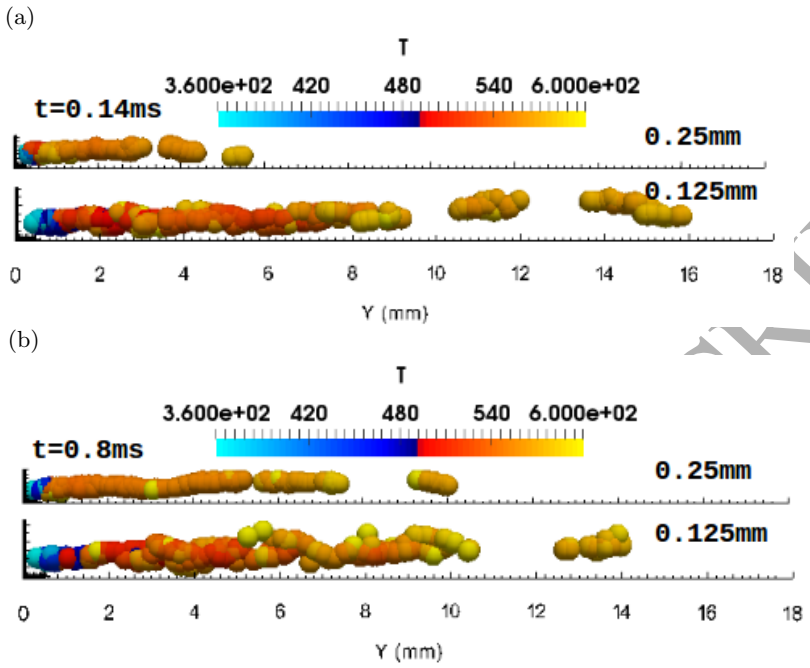

Figure 13: Effect of the grid size on development of particles at $t = 0.8$ms (a) and $t = 1.5$ms (b) for Spray A conditions on mesh 2. The parcels are coloured based on their temperature magnitude.

for both mesh structures and all grid resolutions. We remind that numerically in the current work boiling is accounted through the model presented in Zuo et al., 2000. Another interesting note is that at grid resolution of 0.125 mm the temperature distribution is greater along the liquid core while in the case of larger grid sizes the transitions among the different temperatures is more gradual. This is because in higher grid resolutions more turbulent eddies are resolved which in turn create different temperature gradients locally that affect evaporation and boiling.

Figure 14 shows the total mass transferred due to phase change against time. It can be seen that the amount of fuel mass that undergoes phase change is almost the same at the early stages of fuel injection before $t = 0.2$ ms regardless of the structure of the mesh or the grid size. It is reminded that $t = 0.2$ ms is

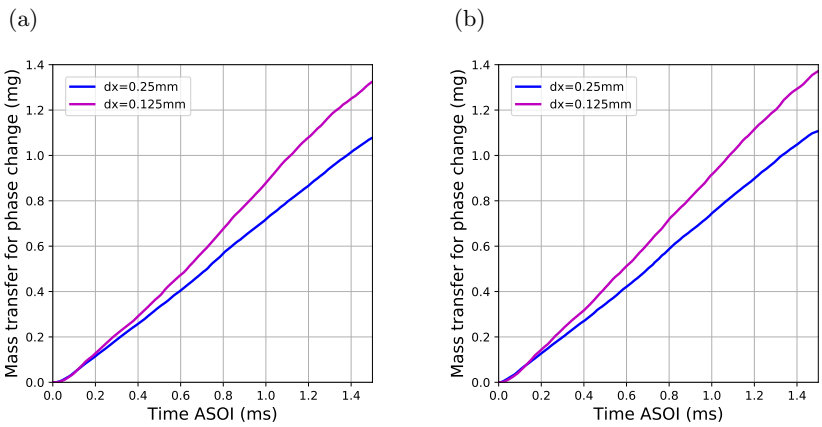

Figure 14: Effect of the grid size on mass transfer for phase change of Spray A conditions for mesh 1 (a) and mesh 2 (b).

the time that is required for the liquid to reach a constant penetration length (Figs 2a and 3a). It is also the duration of the evaporating stage (Figs 12 and 13). After this period the mass transferred is similar with both mesh configurations when the same grid size is used regardless of the fact that for mesh 2 the global SMD of the droplets is smaller than mesh 1. This can be an indication that the rate of the mass that changes phase during the boiling phase does depends mostly on the grid refinement region close to the nozzle and not further downstream.

In order to analyse further the link between the droplet sizes and the phase change dynamics at various locations Figs 15 and 16 are included. They show the number of droplet parcels vs droplet sizes at locations before ($y = 0.5\,\text{mm}$) and after ($y = 3\,\text{mm}$ for mesh 1 and $y = 2\,\text{mm}$ for mesh 2) the boiling position along the spray axis at $t = 0.14\,\text{ms}$ and $t = 0.8\,\text{ms}$. We remind that in reality in the code we deal with "parcels" which are groups of droplets with the same diameter rather than individual droplets. It can be seen that the droplets have larger diameter size before the boiling position, while their sizes are reduced quickly after the boiling position toward their SMD values as shown in Fig. 5. It can also be seen that after the boiling position, and due to effect of breakup

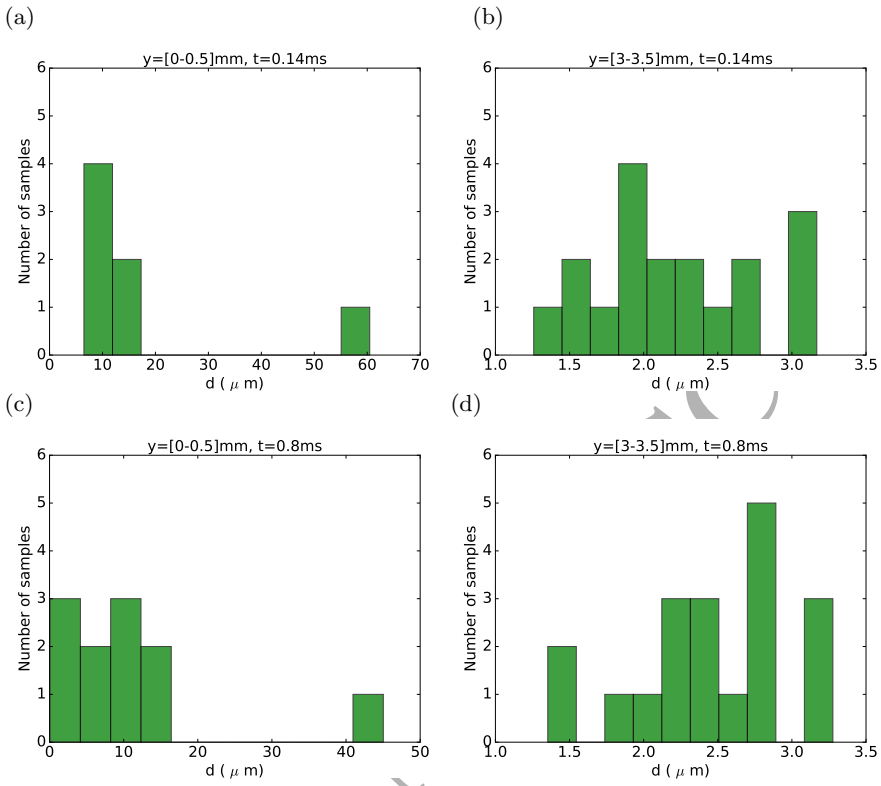

Figure 15: Number of parcel samples vs droplet sizes along the entire radial extent at different time instants and different locations along fuel injection direction (a) $y = 0.5\,\text{mm}$, $t = 0.14\,\text{ms}$ (b) $y = 3\,\text{mm}$, $t = 0.14\,\text{ms}$ (c) $y = 0.5\,\text{mm}$, $t = 0.8\,\text{ms}$ and (d) $y = 3\,\text{mm}$, $t = 0.8\,\text{ms}$ with grid size 0.125 mm of mesh 1.

coefficient B_1, the droplets globally have smaller size and narrower diameter distribution range with mesh 2 than mesh 1. After injection, the liquid fuel is distributed in a range around 0-11mm from nozzle while most of the fuel is transferred into gas due to high temperature and quick breakup process.

4.3. Analysis of gas phase

Figure 17 and 18 display the fuel vapour contours at mid-plane at t= 0.8 ms and 1.5 ms at different grid resolutions for mesh 1 and 2. Although the droplets travel longer as the grid is refined for both meshes, the same trend is noticed for vapour only for mesh 1 while for mesh 2 the grid refinement causes the vapour

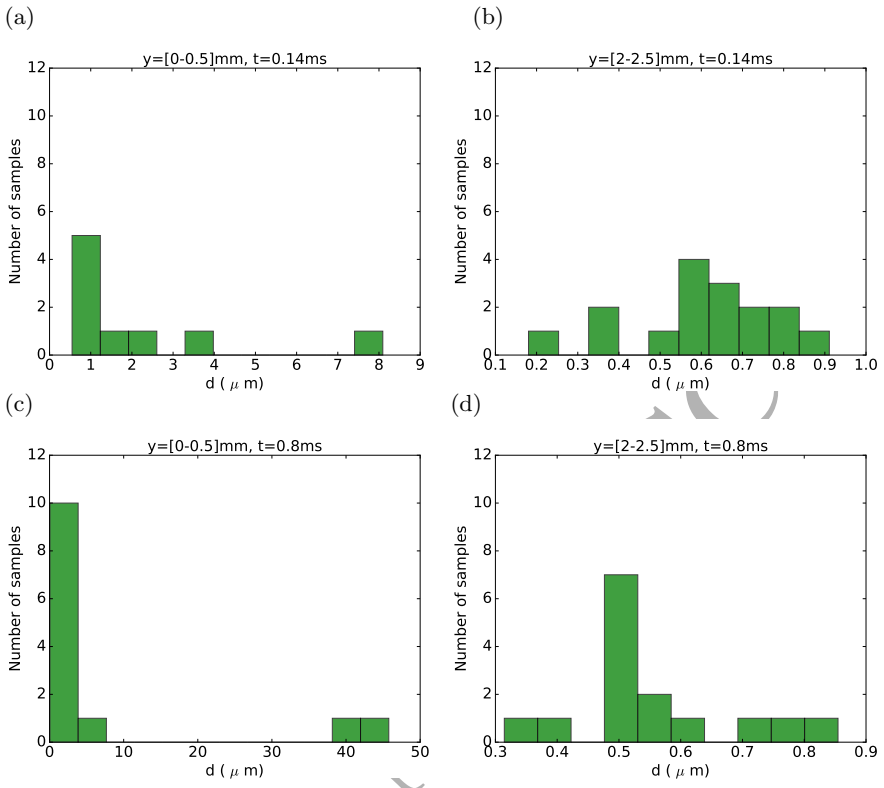

Figure 16: Number of parcel samples vs droplet sizes along the entire radial extent at different time instant and different locations along spray axis (a) $y = 0.5\,\text{mm}$, $t = 0.14\,\text{ms}$ (b) $y = 2\,\text{mm}$, $t = 0.14\,\text{ms}$ (c) $y = 0.5\,\text{mm}$, $t = 0.8\,\text{ms}$ and (d) $y = 2\,\text{mm}$, $t = 0.8\,\text{ms}$ with grid size 0.125 mm of mesh 2.

to diffuse rather than to penetrate. In the interpretation of the results it should be taken into account that although mesh 1 and mesh 2 have exactly the same mesh refinement in the liquid core part (up to 10 mm) their mesh resolution further downstream is different (see Figure 1). At grid resolution 0.25 mm the vapour penetration is longer at mesh 2. At grid resolution 0.125 mm on the other hand the vapour penetration is longer at mesh 1. This behaviour is linked to the effect of small turbulent scales on the process. Although a resolution of 0.125 mm at the liquid core side (up to 10 mm) is adequate to predict global liquid penetrations and total phase change mass, the instantaneous droplet and

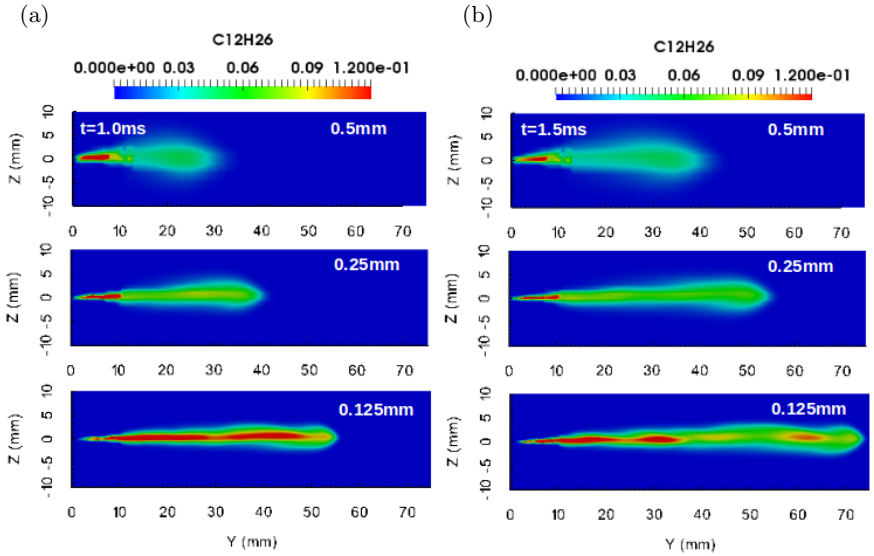

Figure 17: Effect of the grid size on vapour contours at mid-plane $t = 1.5$ ms for for mesh 1.

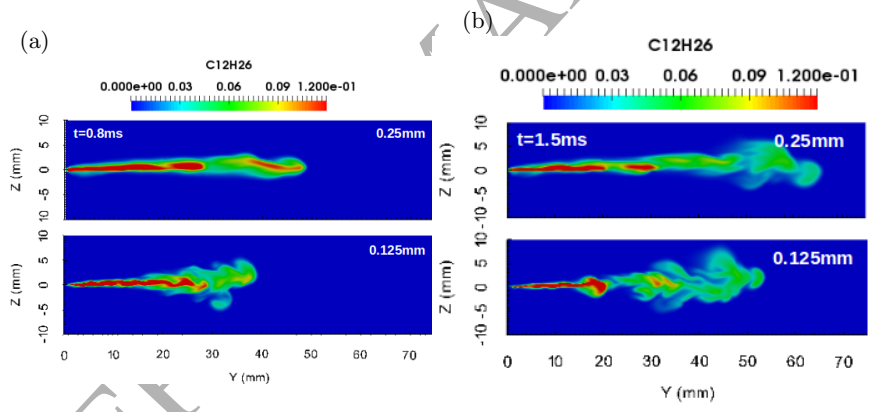

Figure 18: Effect of the grid size on temperature contours at mid-plane $t = 1.5$ ms for mesh 2.

vapour characteristics are greatly affected by the resolution further downstream as well, because of the effect of turbulent eddies on the balance of vapour convection and diffusion. It is estimated that the approximately linear growth trend with decreasing the grid size occurring on liquid penetrations using mesh 1 is mainly a numerical trend dictated by the conservation of momentum (Eq. 12) along the direction of mass flow injection as explained above. On the other

hand, the shorter vapour penetration with the 0.125 mm grid in comparison to 0.25 mm grid resolution for mesh 2, underlines the physical role of the small scales. In mesh 2 more turbulent scales are included further downstream which increase the mixing of the vapour phase with the surrounding gas (N_2).

It is reminded also that based on Table 4 the numerical Stokes numbers for mesh 2 are smaller than for mesh 1, implying that the droplet trajectories are more prone to change because of the local turbulence. There is a stronger coupled effect between the moving particles and gas phase with a smaller Stokes number at mesh 2 and a stronger contribution of moving particles on the source terms that are present into the differential equations of the gaseous phase ($\sum_p m_p((u_p)_{out} - (u_p)_{in})/(V_{cell}\Delta t)$, where $(u_p)_{in}$, $(u_p)_{out}$ are the velocities of particles moving in and out of a cell with volume V_{cell}), when the grid (smaller V_{cell}) is more refined span-wise.

Another important notice in terms of mixture formation ahead of the combustion process is that in mesh 1 the grid refinement leads to pockets of high vapour concentration traveling longer, protected in the core of the spray, while for mesh 2 the vapour is diffused more and thus high fuel vapour mainly exists up to 20 mm at $t = 1.5$ ms. This difference in the vapour distribution is expected to affect the combustion mode that will be observed if reactions are accounted in the simulations. Under the same conditions, the combustion with mesh 1 is expected to be dominated by non/less-premixed mode dynamics while in mesh 2 it will be much sufficiently premixed.

Figures 19 and 20 show the predicted gas-phase temperature with different grid resolutions at two time instants. It can be seen that when comparing different grid resolutions for different meshes important differences are noted. For coarse grid resolution in mesh 1 there is a rather "cold" region up to 10 mm while vapour with rather homogeneous 800 K temperature is noticed further downstream. For mesh 2 in contrast, the "cold" region is longer. For the resolution of 0.125 mm the trend is opposite. The cold vapour travels much longer in mesh 1 than mesh 2. To a certain extent it is expected that the area with the lower temperature should follow the penetrating "cold" liquid

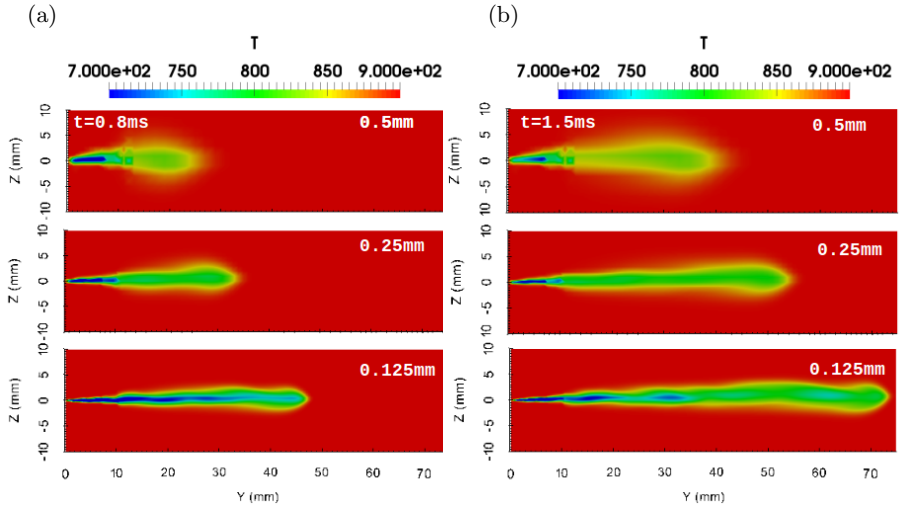

Figure 19: Effect of the grid size on temperature contours at mid-plane $t = 1.5$ ms for mesh 1.

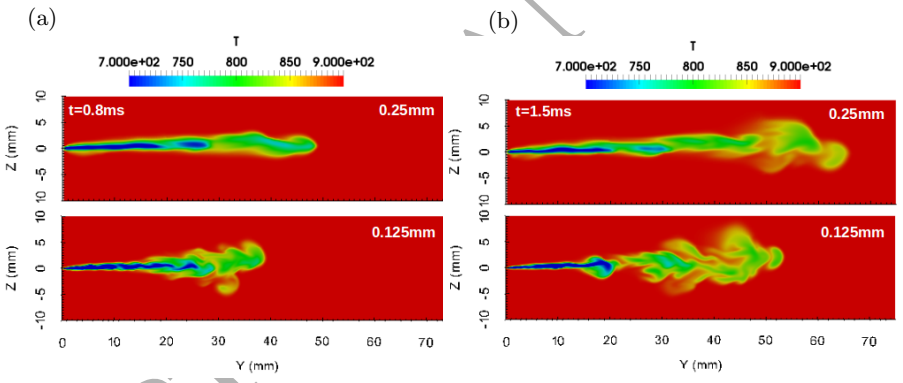

Figure 20: Effect of the grid size on temperature contours at mid-plane $t = 1.5$ ms for mesh 2.

profile. Although indeed droplets penetrate more for mesh 1 this only extends up to 16 mm roughly. Pockets of evaporated vapour (rather than droplets and vapour) travel fast further downstream (up to 40 mm). This is because the area further downstream is less resolved and thus the cold vapour does not mix well with the hot environment.

Flow effects are examined in more detail for 0.125 mm resolution for both mesh 1 and 2 in Fig. 21, which shows the Favre-averaged velocity vectors in

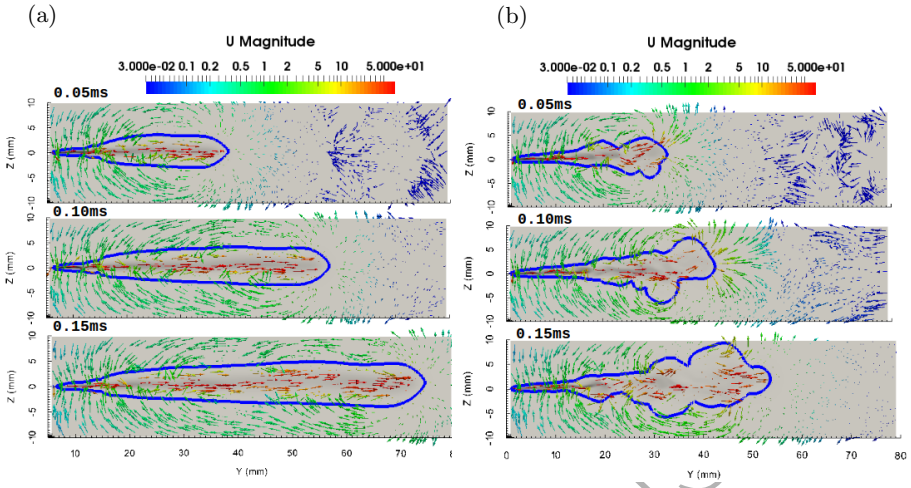

Figure 21: Velocity vectors of (a) 0.125 mm of mesh 1 and (b) 0.125 mm of mesh 2; blue curve: contour of fuel mixture fraction is 0.001.

the periphery of the jet. The contour of the mixture fraction 0.001 is marked as a blue curve to indicate the periphery of the jet. Axial velocities peak (red colour) on the centre line and there is a radially diverging flow around the jet head. The gas entrainment is evident towards the nozzle. Just behind the head of the jet, the combination of the radially diverging flow at the head and the entrainment flow behind creates a counter-clockwise vortex for the upper half region and a clockwise vortex for the lower half region of the computational domain. This feature is also observed in experimental particle image velocimetry (PIV) measurements (Malbec and D'Errico, 2012) and the structure analysis of spray flame (Pei et al., 2016) of the same case.

Also it is interesting to observe the region where diffusion is significant. With mesh 2, the role of diffusion is more noticeable on the head of the jet before the end of injection, while the effect of entrainment is larger than diffusion on mesh 1. This is probably related to the larger linear momentum and linear kinetic energy of the liquid particles with mesh 1 than mesh 2, along the fuel injection direction. At $t = 0.15$ ms with mesh 2, the diffusion effect around the jet head becomes less which is consistent with the end of the injection

time. This feature associated to the transient turbulent nature of the flow inside the combustion chamber importantly affects the non-uniform fuel and air mixing. Subsequently local inhomogeneity in equivalence ratio can result in varied ignition and emission characteristics.

5. Conclusions

The present work is focused on the effect the mesh structure as well as grid size refinement has on spray evaporation and mixture formation in LES using Eulerian-Lagrangian approaches. The grid size overall apart from its profound role on resolving turbulent scales for the Eulerian phase that has been explored in previous studies, also affects the way the droplets move and evaporate both because of the physics of the flows that are reproduced as well as the code numerics. Although for this work we used as the basis of the analysis fuel spray simulations of n-dodecane under non-reacting conditions injected in a high pressure, high temperature constant chamber known as "Spray A" conditions, it should be underlined that the above conclusion can be generalised to any other high speed evaporating spray. The main conclusions can be summarised as following

1. Although previous studies have provided suggestions for the grid size that should be used in spray simulations the suggestions are case specific and are based on a "trial and error basis" without providing any rigorous selection procedure. As it is clear from our analysis that the selected grid size and accuracy of the results is dependent both on the mesh structure as well as the code numerics and the SGS models. Thus, there is not a unique "optimum" grid that should be used for a given set of experimental data.
2. We observe that as the grid is refined, the results for global liquid and vapour penetration demonstrate convergence toward the experimental data. However, this is not necessarily indicative of the overall accuracy of the

simulations since -depending on the refinement areas- the droplet statistics are altered. More experimental data relevant to droplet sizes and velocities are required though for more solid conclusions.

3. For both mesh cases examined in this study, as the grid size close to the liquid core area is refined the droplet trajectories are becoming longer (higher liquid penetration) and more fuel droplets with higher velocities are present in the domain.
4. For the vapour penetration the trend that the vapour length follows as the grid is refined depends considerably on the mesh structure. The mesh refinement along the direction of mass flow injection allows for more small scales to be included, which also alters the temperature and velocity distribution around the liquid which in turn affects the droplet size distribution and the overall droplet number. The overall mass exchanged does not change.
5. The grid size -if a variable Co number is used- affects the numerical time step which in turn affects how "often" the gas momentum equation is updated in respect to the time steps of the liquid phase and this can impose numerical oscillations for the prediction of the vapour phase.
6. We calculated the Stokes numbers in all examined cases and we found that they are less than 1, indicating that the particles' motions are tightly coupled to the motion of gas phase. This makes the calculations very prone to the selection of B_1 since the particle break up enhances this coupling.
7. It was found that the droplet SMDs follow a linear relation in respect to the B_1 which is particularly helpful in order to a priori select the coefficient in various high speed evaporating sprays if the experimental droplet size or the experimental Stokes number is known.
8. The Stokes numbers were found to be smaller with mesh 2 than mesh 1. This implies a stronger coupling of the two phases for mesh 2 and the dynamics of the liquid (Lagrangian) phase are considerably influenced by the numerical and physical instabilities of the gas (Eulerian) phase.
9. Since for multiphase flows the Kolmogorov scale cannot be considered as

the only smallest flow scale and be used as scale separation criterion for the grid selection in a similar way done for single phase flows, the numerical Stokes number can play the role of an additional grid selection parameter.

6. Acknowledgements

This work was supported by the UK's Engineering and Physical Science Research Council through grant EP/P012744/1.

References

Amsden, A. A., Orourke, P. J. and Butler, T. D. 1989, 'KIVA-II : A computer program for chemically reactive flows with sprays', *NASA STI/Recon Technical Report N* **89**.

Bailey, A. G., Balachandran, W. and Williams, T. J. 1983, 'The rosin-rammler size distribution for liquid droplet ensembles', *Journal of Aerosol Science* **14**(1), 39–46.

Banerjee, S. and Rutland, C. 2012, On LES grid criteria for spray induced turbulence, *in* 'SAE Technical Paper Series', SAE International.

Battistoni, M., Xue, Q. and Som, S. 2015, 'Large-eddy simulation (LES) of spray transients : start and end of injection phenomena', *Oil & Gas Science and Technology – Revue d'IFP Energies nouvelles* **71**(1), 4.

Beck, J. C. and Watkins, A. P. 2003, 'On the development of a spray model based on drop-size moments', *Proceedings of the Royal Society A: Mathematical, Physical and Engineering Sciences* **459**(2034), 1365–1394.

Blokkeel, G., Barbeau, B. and Borghi, R. 2003, A 3D eulerian model to improve the primary breakup of atomizing jet, *in* 'SAE Technical Paper Series', SAE International.

Blomberg, C. K., Zeugin, L., Pandurangi, S. S., Bolla, M., Boulouchos, K. and Wright, Y. M. 2016, 'Modeling split injections of ECN "spray a" using a conditional moment closure combustion model with RANS and LES', *SAE International Journal of Engines* **9**(4).

Bravo, L. and Kweon, C. B. 2014, 'Numerical simulations of evaporating sprays in high pressure and temperature operating conditions'.

Gong, Y., Kaario, O., Tilli, A., Larmi, M. and Tanner, F. X. 2010, A computational investigation of hydrotreated vegetable oil sprays using RANS and a modified version of the RNG k - ϵ model in OpenFOAM, *in* 'SAE Technical Paper Series', SAE International.

Jangi, M., Solsjo, R., Johansson, B. and Bai, X.-S. 2015, 'On large eddy simulation of diesel spray for internal combustion engines', *International Journal of Heat and Fluid Flow* **53**, 68–80.

Kim, W.-W. and Menon, S. 1995, A new dynamic one-equation subgrid-scale model for large eddy simulations, *in* '33rd Aerospace Sciences Meeting and Exhibit', American Institute of Aeronautics and Astronautics, Reno, NV, USA.

Lucchini, T., D'Errico, G., Ettorre, D. and Ferrari, G. 2009, 'Numerical investigation of non-reacting and reacting diesel sprays in constant-volume vessels', *SAE International Journal of Fuels and Lubricants* **2**(1), 966–975.

Magnotti, G. and Genzale, C. 2017, 'Detailed assessment of diesel spray atomization models using visible and x-ray extinction measurements', *International Journal of Multiphase Flow* **97**, 33–45.

Malbec, L.-M. and D'Errico, G. 2012, 'Mixing and velocity session'.
URL: *https://ecn.sandia.gov/ecn-workshop/ecn2-proceedings/*

Pei, Y., Hu, B. and Som, S. 2016, 'Large-eddy simulation of an n-dodecane spray flame under different ambient oxygen conditions', *Journal of Energy Resources Technology* **138**(3), 032205.

Pickett, L. M., Genzale, C. L., Bruneaux, G., Malbec, L.-M., Hermant, L., Christiansen, C. and Schramm, J. 2010, 'Comparison of diesel spray combustion in different high-temperature, high-pressure facilities', *SAE International Journal of Engines* **3**(2), 156–181.

Pomraning, E. 2000, Development of large eddy simulation turbulence models, PhD thesis, University of Wisconsin - Madison.

Pomraning, E. and Rutland, C. J. 2002, 'Dynamic one-equation nonviscosity large-eddy simulation model', *AIAA Journal* **40**, 689–701.

Ranz, W. E. and W. R. Marshall, J. 1952*a*, 'Vaporation from drops, part 1', *Chem. Eng. Prog.* **48**, 141–146.

Ranz, W. E. and W. R. Marshall, J. 1952*b*, 'Vaporation from drops, part 2', *Chem. Eng. Prog.* **48**, 173–180.

Reitz, R. 1987, 'Modeling atomization processes in high-pressure vaporizing sprays', *Atomisation Spray Technology* **3**, 309–337.

Rutland, C. J. 2011, 'Large-eddy simulations for internal combustion engines a review', *International Journal of Engine Research* **12**(5), 421–451.

Sandia National Laboratories 2018, 'Engine combustion network', `https://ecn.sandia.gov/`.

Schmidt, D. P. and Bedford, F. 2018, 'An analysis of the convergence of stochastic lagrangian/eulerian spray simulations', *International Journal of Multiphase Flow* **102**, 95–101.

Senecal, P. K., Mitra, S., Pomraning, E., Xue, Q., Som, S., Banerjee, S., Hu, B., Liu, K., Rajamohan, D. and Deur, J. M. 2014, Modeling fuel spray vapor distribution with large eddy simulation of multiple realizations, *in* 'Volume 2: Instrumentation, Controls, and Hybrids Numerical Simulation Engine Design and Mechanical Development Keynote Papers', ASME.

Senecal, P. K., Pomraning, E., Richards, K. J., Briggs, T. E., Choi, C. Y., Mcdavid, R. M. and Patterson, M. A. 2003, Multi-dimensional modeling of direct-injection diesel spray liquid length and flame lift-off length using CFD and parallel detailed chemistry, *in* 'SAE Technical Paper Series', SAE International.

Senecal, P. K., Pomraning, E., Xue, Q., Som, S., Banerjee, S., Hu, B., Liu, K. and Deur, J. M. 2013, Large eddy simulation of vaporizing sprays considering multi-injection averaging and grid-convergent mesh resolution, *in* 'Volume 2: Fuels Numerical Simulation Engine Design, Lubrication, and Applications', ASME.

Senecal, P. K., Richards, K. J., Pomraning, E., Yang, T., Dai, M. Z., McDavid, R. M., Patterson, M. A., Hou, S. and Shethaji, T. 2007, A new parallel cut-cell cartesian CFD code for rapid grid generation applied to in-cylinder diesel engine simulations, *in* 'SAE Technical Paper Series', SAE International.

Som, S. and Aggarwal, S. 2010, 'Effects of primary breakup modeling on spray and combustion characteristics of compression ignition engines', *Combustion and Flame* **157**(6), 1179–1193.

Som, S., D'Errico, G., Longman, D. and Lucchini, T. 2012, Comparison and standardization of numerical approaches for the prediction of non-reacting and reacting diesel sprays, *in* 'SAE Technical Paper Series', SAE International.

Som, S., Senecal, P. and Pomraning, E. 2012, Comparison of RANS and LES turbulence models against constant volume diesel experiments, *in* '24^{th} Annual Conference on Liquid Atomization and Spray Systems', ILASS Americas, San Antonio, Texas, USA.

Spalding, D. B. 1964, 'Convective mass transfer–an introduction', *AIChE Journal* **10**(3), 290–425.

Vallet, A., Burluka, A. A. and Borghi, R. 2001, 'Development of a eularian model for the "atomization" of a liquid jet', *Atomization and Sprays* **11**(6), 24.

Vogiatzaki, K., Crua, C., Morgan, R. and Heikal, M. 2017, A study of the controlling parameters of fuel air mixture formation for ECN spray a, *in* 'Proceedings ILASS–Europe 2017. 28th Conference on Liquid Atomization and Spray Systems', Universitat Politècnica València.

Vujanović, M., Petranović, Z., Edelbauer, W. and Duić, N. 2016, 'Modelling spray and combustion processes in diesel engine by using the coupled eulerian–eulerian and eulerian–lagrangian method', *Energy Conversion and Management* **125**, 15–25.

Wehrfritz, A., Vuorinen, V., Kaario, O. and Larmi, M. 2012, A high resolution study of non-reacting fuel sprays using large-eddy simulations, *in* 'ILASS Americas, 12^{th} Triennial International Conference on Liquid Atomization and Spray Systems', Heidelberg, Germany.

W.P., J., A.J., M. and K., V. 2014, 'Large-eddy simulation of spray combustion in a gas turbine combustor', *Combustion and Flame* **161**(1), 222 – 239.

Xue, Q., Som, S., Senecal, P. K. and Pomraning, E. 2013, A study of grid resolution and SGS models for LES under non-reacting spray conditions, *in* 'ILASS Americas, 25^{th} Annual Conference on Liquid Atomization and Spray Systems', Pittsburgh, USA.

Yi, Y. and Reitz, R. D. 2003, Modeling the effect of primary atomization on diesel engine emissions, *in* 'SAE Technical Paper Series', SAE International.

Zamani, H., Hosseini, V., Afshin, H., Allocca, L. and Baloo, M. 2016, 'Large eddy simulation of GDI single-hole and multi-hole injector sprays with comparison of numerical break-up models and coefficients', *Journal of Applied Fluid Mechanics* **9**(2), 1013–1022.

Zhou, L., Xie, M.-Z., Jia, M. and Shi, J.-R. 2011, 'Large eddy simulation of fuel injection and mixing process in a diesel engine', *Acta Mechanica Sinica* **27**(4), 519–530.

Zuo, B., Gomes, A. M. and Rutland, C. J. 2000, 'Studies of superheated fuel spray structures and vaporization in gdi engines', *International Journal of Engine Research* pp. 321–336.

Appendices

A. LES and Spray Sub-Gird Scale Models

A.1. Injection model

The injection process is simulated using a cone injection model. The spray is represented by an ensemble of discrete "parcels". A Rosin-Rammler distribution (Bailey et al., 1983) predicts the mass fraction $f(d)$ of particles having sizes greater than the diameter d as

$$f(d) = (d/d_0)^n e^{(-d/d_0)^n} \tag{13}$$

The exponent n affects the spread of the distribution and d_0 is a parameter affecting the mean particle size of distribution. The numerical values $n = 3$ and $d_0 = 90\mu m$ are implemented in present work. The injected droplets have a diameter in the range $1\mu m \leq d \leq 90\mu m$. An initial spray spreading angle has been prescribed as 21.50^0 after sensitivity analysis and literature review.

A.2. The break-up model

The liquid jet break-up is known to be caused by the KelvinHelmholtz (KH) and Rayleigh Taylor (RT) instabilities at the interface of the two fluids. The KHRT model was first proposed by Reitz Reitz 1987 and it is a combination of the KH model and the assumption of occurring RT instabilities at the droplet

surface. The KH breakup mechanism assumes the droplets to behave like a liquid jet injected into an incompressible gas environment. The liquid surface is therefore subject to small perturbations that are amplified by the liquidgas phase interaction which leads to small droplets stripped off from the surface. Based on the perturbation growth rate Ω_{KH} and wavelength Λ_{KH} a breakup time and droplet diameter can be determined. Reitz gives correlation obtained from curve-fits to the analytic solution for the wavelength and growth rate. The breakup time is than given by

$$\tau_{KH} = 3.726 B_1 \frac{r}{\Lambda_{KH}\Omega_{KH}} \tag{14}$$

where r denotes the radius of the initial droplets. The break-up parameter influences the rate of separation and depends on the nozzle and the spray's properties. The values of $B_1 = 3$, and 15, are adopted for simulations using mesh 2 and mesh 1 respectively in Fig. 1. The RT model is based on theoretical considerations on the stability of liquid-gas interfaces that are accelerated in normal direction. Assuming a linear disturbance growth a growth rate and wavelength can be determined. The breakup time is thus obtained by the reciprocal of the growth rate and a correction factor C_τ to delay the breakup under certain conditions as

$$\tau_{RT} = C_\tau \frac{1}{\Omega_{KH}} \tag{15}$$

Droplet break-up is encountered if $d_d > \Lambda_{RT}$ and τ_{RT} is greater than the time of disturbance growth. Both mechanisms, KH and RT, are implemented in a competing manner to determine the final droplet break-up.

The parameters of KHRT model adopted in our study are given in the following table.

A.3. Dynamic one-equation eddy viscosity model

In our work, a dynamic one-equation eddy viscosity model (Kim and Menon, 1995) is adopted by solving the transport equation for subgrid-scale kinetic energy as

B_0	0.61
B_1 (adjustable between 1.73-60)	3, 15
Ctau	1
CRT (adjustable between 0.05-2)	0.1
msLimit	0.2
WeberLimit	6

Table 5: The parameters of KHRT model used in the present work.

$$\frac{\partial \widetilde{k}_{sgs}}{\partial t} + \frac{\partial}{\partial x_j}(\widetilde{u}_j k_{sgs}) = -\tau_{ij}\frac{\partial \widetilde{u}_i}{\partial x_j} - \varepsilon_{sgs} + \frac{\partial}{\partial x_j}(\mu_t \frac{\partial k_{sgs}}{\partial x_j}) \tag{16}$$

where

$$\mu_t = C_\tau \Delta k_{sgs}^{1/2}, \varepsilon_{sgs} = C_\varepsilon \frac{k_{sgs}^{3/2}}{\Delta} \tag{17}$$

the subgrid-scale stress can be expressed as

$$\tau_{ij} = -2C_\tau \Delta k_{sgs}^{1/2}\widetilde{S}_{ij} + \frac{2}{3}\delta_{ij}k_{sgs} \tag{18}$$

the dynamic procedures are employed to evaluate C_τ and C_ε using a test filter field (typically, $\Delta' = 2\Delta$) constructed from the grid-scale field. The model coefficient is amended spatially and temporally, subsequently an accurate local effect of the small scales is applied on the LES flow field.

B. Zoom in of the area up to 2 mm penetration

Figure 22 shows the injected parcels (at t=1.0ms) have bigger sizes close to nozzle, although it can not show a standard Rosin-Rammler distribution, because the fuel parcels are disintegrated rapidly after injected into the high temperature chamber due to a quick primary breakup and evaporation.

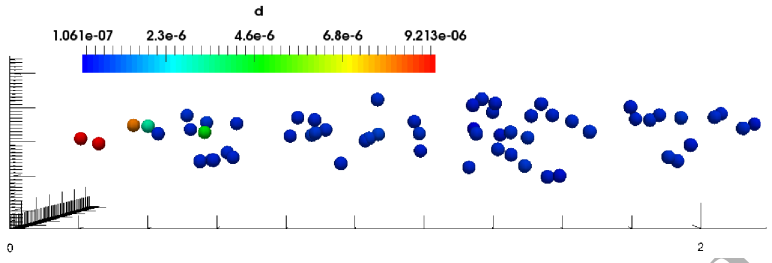

Figure 22: Particels close to nozzle for simulation with mesh 2 size 0.125mm at $t = 1.0ms$.

C. Particle independence study

Figure 23 shows the oscillation/noise magnitudes of the liquid penetrations are almost the same order by increasing the PPS number from 30, 40, 50, 80 to 100 million. The best matching of simulated vapor penetration against the experimental data occurs at PPS=40 million which is the number used in this study.

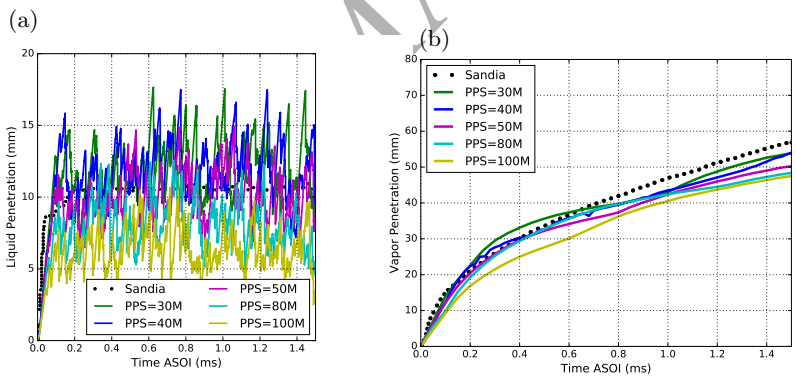

Figure 23: Liquid (a) and vapour (b) penetrations with PPS=40M, 80M and 100M, for simulations with mesh size 0.125mm of mesh 2.

D. Sensitivity analysis of the B_1 parameter

Figure 24 displays the simulation results with mesh size 0.125 mm of both mesh structures, mesh 1 using B_1=3 (matching value for mesh 2), and mesh 2

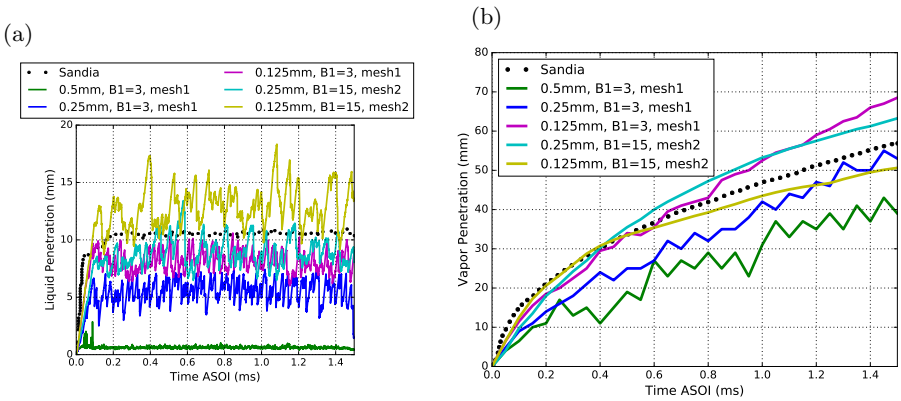

Figure 24: Liquid (a) and vapour (b) penetrations for simulations using $B_1 = 3$ on mesh1 and $B_1 = 15$ on mesh 2.

using B_1=15 (matching value for mesh 1). The results show that the simulated liquid and vapour penetrations are less convergent against the experimental data, when a mismatched B_1 is used.